



Droplet Growth Dynamics during Atmospheric Condensation on Nanopillar Surfaces

Mohammad Rejaul Haque^a, Chuang Qu^b, Edward C. Kinzel^b, and Amy Rachel Betz^a

^aMechanical and Nuclear Engineering, Kansas State University, Manhattan, KS, USA; ^bMechanical and Aerospace Engineering, Missouri University of Science and Technology, Rolla, MO, USA

ABSTRACT

The Gibbs free energy barrier for heterogeneous nucleation of a condensed droplet on a rough surface changes significantly with changes of humidity content in the condensing environment. The influence of environmental factors (ambient temperature and relative humidity) and substrate characteristics (topology, surface chemistry, and substrate temperature) on atmospheric condensation phenomenon is very important to elucidate the condensed droplet wetting state and condensate harvesting applications. Condensation from the humid air has been reported for plain silicon and fabricated nanopillar surfaces to facilitate condensate harvesting. Droplet growth and size distributions were recorded for 90 min. Spherical droplets condensed on the silicon surfaces and irregular-shaped droplets were observed on the nanopillar surfaces due to the pinning effect of the pillars. The effect of droplet pinning on coalescence events has been described based on the energy balance for the condensed droplets. A mathematical model reveals that certain dimensional combinations (pillar pitch, pillar diameter, and pillar height) of the nanopillar geometry are required to exhibit the pinning mechanism for condensed droplets. Regeneration of droplets was observed at void spaces generated from coalescence events. The growth of individual droplets was tracked over multiple time and length scales, starting from nucleation to get further insight into the direct growth and coalescence mechanisms.

Abbreviation: ESEM: Environmental Scanning Electron Microscope; HCP: Hexagonal Closed-Packed; MPL: Microsphere Photolithography; RH: Relative Humidity

ARTICLE HISTORY

Received 15 October 2017 Accepted 20 June 2018

KEYWORDS

Atmospheric condensation; droplet dynamics; coalescence; nanopillar; pinning effect

Introduction

At atmospheric pressure, a surface below the dew point temperature for a certain relative humidity generates water droplets on the surface. This atmospheric phenomenon is very important in applications such as energy harvesting, water desalination or distillation, and other systems where water collection and frequent droplets shedding occur. The field of dropwise condensation has been investigated for many years [1, 2]. Early studies concluded the droplet growth procedure as self-similar [2]. The role of coalescence in the droplet growth dynamics was not included in the early models. Droplet growth and size distribution at atmospheric pressure are still difficult to predict for the engineered surfaces, especially in the presence of mixtures such as humid air. Condensation experiment was studied for transient flow dynamics and droplet dynamics [3–5]. Numerical modeling of the droplet growth mechanism was investigated [6–8]. The condensation phenomenon is significantly affected by the environmental factors and surface morphologies [9], superhydrophobic

CONTACT Amy Rachel Betz arbetz@ksu.edu 3002 Rathbone Hall, 1701B Platt St, Manhattan, KS 66506, United States Color versions of one or more of the figures in the article can be found online at www.tandfonline.com/umte.

B Supplemental data for this article can be accessed here.

coated surfaces [10–13], low thermal conductive surface [14], the pressure of steam and the size distribution of the droplet [14, 15], and hydrophobic surfaces [16, 17]. The self-propelling motion of the droplets [18] also alters the growth dynamics. Experiments were carried out for biphilic surfaces [19], superhydrophobic surfaces [20–23], different textured surfaces [24], and also for capillary and wettability gradient surfaces [25]. The condensing droplets penetrate the surface texture and micro patterned hydrophobic surface allows better self-cleaning property. Nanotextured superhydrophobic surfaces showed the mobility of small 100 µm droplets [26]. A droplet coalescence mechanism in environmental scanning electron microscopy (ESEM) imaging was developed [27] and the temporal size distribution of droplets was also investigated [28]. Surface chemistry to induce hydrophobicity, the scalable coating, the impact of surface texture for droplet mobility, and the multiscale surface texture for enhancing droplet mobility was clearly demonstrated [29–31]. Therefore, it clearly indicates the importance of surface engineering on dropwise condensation heat transfer. For the nucleation of droplets [32, 33, and S1], Gibbs free energy change of heterogeneous nucleation energy barrier can be expressed as follows:

$$\Delta G_{heterogenous} = \Delta G_{hom ogenous} \times s(\theta')$$

$$\Delta G_{heterogenous} = \left[-\frac{4}{3} \pi \rho_d R_m T ln(\frac{e}{e_s}) R^3 + 4\pi \gamma R^2 \right] \times s(\theta')$$
(1)

$$X = -\frac{4}{3}\pi\rho_d R_m T \ln(\frac{e}{e_s})$$

$$Y = 4\pi \gamma$$

$$\Delta G_{heterogenous} = [XR^3(a) + YR^2(b)] \times s(\theta')$$
 (2)

$$s(\theta') = \frac{(2 + \cos \theta')(1 - \cos \theta')^2}{4} \tag{3}$$

In the case of heterogeneous nucleation of a droplet, the nucleation energy barrier is less than the homogeneous nucleation energy barrier as the $s(\theta')$ value from Equation (3) varies between 0 and 1. For hydrophobic or lower energy surfaces, the nucleation energy barrier is higher than higher energy surfaces. Total free energy change depends on two terms depicted in Equation (2) namely bulk free energy difference between the vapor and the liquid (a), and interfacial free surface energy (b) for the creation and displacement of surfaces involved in the nuclei formation. If a droplet is in equilibrium at radius R, then a condensation of a small quantity of vapor around the droplet will increase the radii and it continues to grow. For the same surface, the energy required to form a nuclei can be obtained from the Gibbs free energy change. Equation (2) illustrated the importance of relative humidity during the condensation dynamics for heterogeneous nucleation of droplets. The relative humidity (RH) has a significant impact on the droplet formation and their subsequent growth as it can manipulate the nucleation energy barrier significantly. For instance, if the experimental chamber is maintained at fixed temperature T, considering the same apparent contact angle (θ') and radius (R) of the initial nuclei formation under 40% RH and 60% RH, the bulk energy factor X of Equation (2) can be increased by approximately 80% for changing the RH to 40% from 60%. It suggested, less energy is required to overcome the nucleation energy barrier for forming nuclei if the experiments are operated at higher humidity and it might be favorable for larger condensate harvesting. This importance of variation of relative humidity is considered as one of the crucial variables in the present research for the condensation experiment. Several studies have been carried out in pure vapor condition neglecting the presence of pure atmosphere [32, 33]. The presence of non-condensable gases in the humid chamber can exhibit additional heat and mass transfer resistance to heat transfer during the droplet formation [34] and

dropwise condensation largely dependent on thermal resistance which can be altered by the presence of non-condensable gases rather than geometric features [35]. Recently, a study [36] has been carried out considering the effect of non-condensable gases in heterogeneous water nucleation to elucidate the presence of sulfur-based volatile organic compounds and aerosols in the atmosphere for agglomerate growth dynamics and its subsequent impact on hydrophobic coating longevity during condensation/ evaporation cycle. In real applications, frost formation is initiated by the formation of condensate droplet from the air-vapor mixture where non-condensable gases (compounds in air) are found [37]. Moreover, optical microscopy has the advantages to validate the droplet growth data against numerical scheme as well as considering the effect of non-condensable content of the saturated vapor [19]. Optical microscopy yields better image quality at higher vapor pressure [13]. Additionally, one practical factor for the implementation of textured surfaces at industrially significant scales is the expense of manufacturing the surface. Using conventional lithography is possible for larger diameter (several micrometer surfaces). Patterning smaller features can be accomplished using advanced lithographic techniques as well e-beam lithography of focused ion-beam milling. Although advanced direct-write techniques such as e-beam lithography, focused ion-beam milling, and two-photon absorption allow prototyping of surfaces with feature sizes below 200 nm, they do not scale well to m² areas. Other emerging patterning technologies such as interference lithography or nanoimprint lithography, have stringent requirements for planarity, pristine surfaces, or use expensive masks. The different techniques are available such as Nanosphere Lithography [38] or Microsphere Photolithography [MPL] [39-42]. On the other end of the length scale, techniques such as anodized alumina templating or block copolymers produce smaller (sub-100 nm features). Several techniques have been developed around the self-assembly of microspheres to form Hexagonal Close-Packed (HCP) monolayers on a substrate. The HCP microsphere arrays can be used as a shadow mask for evaporation (Nanosphere Lithography) or as optical elements to focus incident radiation to sub-wavelength photonic jets (Microsphere Photolithography). These approaches have been widely studied to create plasmonic substrates for Surface Enhanced Raman Spectroscopy (SERS) and metasurfaces but have not previously been used to modify the wettability of surfaces extensively. The advantage of these techniques is low-cost large area patterning of sub-micron structures. In this research, the condensation from air-vapor mixture running the optical microscopy experiments in humidity controlled chamber closer to the operating conditions in industrial applications (ambient pressure and air-vapor mixture, presence of non-condensable compounds in the atmosphere) for natural convection of air flow have been conducted instead of doing it in ESEM. The videos and images of droplet growth dynamics have been reported on plain silicon and nano-patterned surfaces created by MPL. The mechanism of droplet growth was explored via successive images analysis. Thus, the importance of relative humidity combined with fabricated nanopillar surface has been studied in condensation test. The application of this nanopillar surface in condensate water recovery [43, 44] has also been revealed.

Experimental section

Sample fabrication and experimental setup

In this work, Microsphere Photolithography (MPL) has been introduced to generate silica nanopillars on a silicon surface. The MPL method is more effective for large applications such as condensate harvesting over a large area. The manufacturing method introduced in this work can be more scalable and cheap with better precision. The technique is robust and versatile. The use of MPL technique creates surface consisting of silica nanopillars on a silicon substrate. MPL was used to pattern the nanopillar surface as shown in Figure 1. This process uses a self-assembled microsphere array as an optical element to focus flood illumination into a layer of photoresist. Each microsphere collects incident collimated illumination and focuses it onto a sub-diffraction limited photonic jet. At normal incidence, the photonic jet is centered under the microsphere. The MPL technique combines elements of bottom-up (self-assembly) with top-down hierarchical patterning (control of the illumination intensity and angle of incidence). The samples were created by depositing a thick layer of

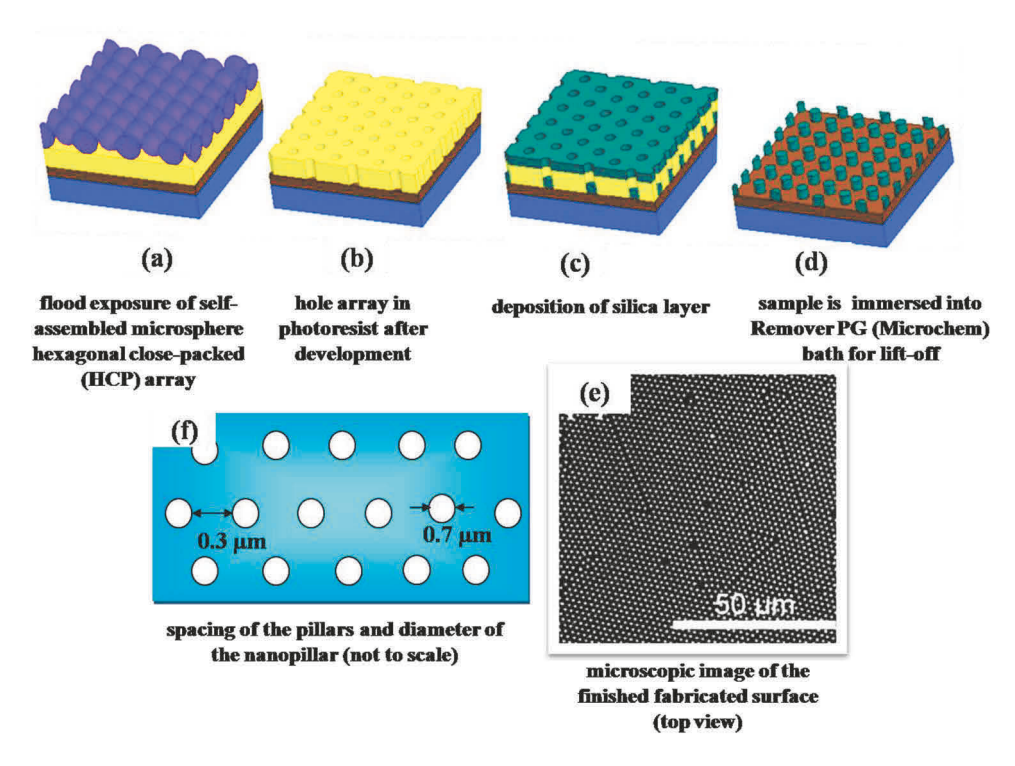


Figure 1. Microsphere photolithography process showing the detailed and sequential fabrication process of silica nanopillar (dark green) on the silicon substrate (brown). The yellow color is for "Photoresist."

silicon onto glass microscope test slides using e-beam evaporation. Adhesion promoter (HDMS, Silicon Resources) and photoresist (S1805, Shipley) were spun onto the silicon surface. The thickness of the photoresist after soft baking is 300 nm. Microspheres were then drop coated (convective selfassembly) onto the photoresist. The samples were flood illuminated using a monochromatic i-line mercury arc lamp as the light source (Bacher and Associates) with the intensity of ~12.5 mW/cm² for different durations. Development in MF319 (Dow) removes the exposed photoresist as well as the microspheres, to reveal a uniform hole array. SiO₂ was then e-beam evaporated onto the sample. After the deposition of SiO₂ onto samples with hole arrays in photoresist, the samples are immersed in Remover PG (Microchem) bath for lift-off. Ultrasonication accelerated the lift-off process. This technique allows stripping the silica deposited onto the photoresist to produce a uniform array of silica pillars on a silicon substrate. The nanopillar surface has three parameters that are controllable using the MPL process; the periodicity (p) determined by the microsphere diameter, the pillar radius (r) determined by the duration of the exposure, and the pillar height (h) determined by the evaporation thickness. In this study, the height of the pillar is ~300 nm and the exposure duration is set to 1 s for a dosage of~12.5 mJ. All of the pillars are arranged in hexagonal close-packed arrays. The price of silica microspheres is ~\$20/g, and 1 g of 2 µm silica microspheres can be used for paving an area over 0.4 m². Regular monochromatic UV light source (such as mercury lamp) can be used in the exposure process. Different from e-beam lithography, MPL is a parallel process for feature generation and all features generated in the photoresist are obtained from a single exposure.

After fabrication and perfect cleaning of the nanostructured surface and plain silicon wafer, apparent contact angle measurements of injected water droplet were conducted primarily to characterize the wetting behavior of the surfaces. Later, the measured apparent contact angle was compared to the recent theoretical model provided in Suzuki et al. [45]. For condensation test, samples were placed on a Peltier device and secured with a small amount of thermal paste on a

condensation stage in a computer controlled chamber at IER. An Omega RHXL3SD thermometer/ hygrometer was used to control the relative humidity and constant air temperature (295 \pm 0.5K) in the experimental chamber. The condensation stage consists of an aluminum heat sink where icewater mixture was circulated from a pump (Fisher Scientific FH100D peristaltic) below a Peltier cooler and the temperature was controlled by a TE Technologies TC-720 temperature controller as shown in Figure 2. The stage was cooled to 278 \pm 0.5K and was monitored by thin film Omega thermocouple connected to Data Acquisition (DAQ) system. The relative humidity (RH) was set at 40% RH and 60% RH respectively. The maximum uncertainty in RH measurement was \pm 2%. The surface temperature was kept at 278 \pm 0.5 K, which was 9 \pm 0.5 K (40% RH) and 3 \pm 0.5 K (60% RH) below the dew point temperature for the considered environmental conditions. This manipulates the nucleation energy barrier and nucleation site density significantly to alter the droplet growth. However, the presence of non-condensable gases might reduce the net driving force or thermal gradient ($T_{sat} - T_l$) for heat transfer of every droplet by adding a diffusion resistance to the vapor-air boundary layer [46].

All the images and videos were captured by a Leica DVM2500 microscope with a maximum resolution of $2500\times$. This allows capturing images of droplets whose initial diameter is around 1–2 μ m. At least three trials were conducted for each combination of surface and relative humidity. The image analysis was done using the built-in software embedded in the Leica microscope. Droplets on the periphery of the image were included in the total droplet count if the visible size of the partial droplets was comparable to other droplets of the frame. The maximum uncertainty for a single droplet diameter measurement is 6.5 pixels, corresponding to $\pm 0.5~\mu$ m.

Results and discussion

Wetting state of the injected and condensed droplet on the fabricated sample

The theoretical model described by Suzuki *et al.* [45] considers the pinning effect at the edge of the pillar. The model represents the apparent contact angle as a function of pillar pitch, pillar width, pillar height, and the forces acting at all interfaces of the droplet. This pinning force significantly affects the wetting state of the droplets as shown in Figure 3a. This model has been modified based

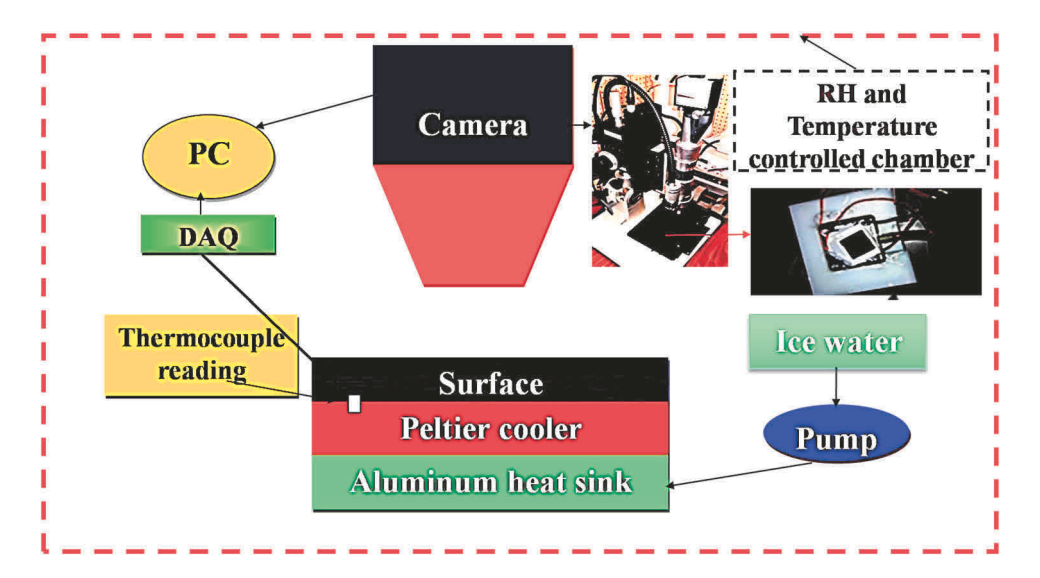


Figure 2. Schematic of the experimental setup in a humidity controlled chamber. The chamber was maintained at atmospheric pressure.

on the surface material and geometry considered in the present study as shown in Equation (6) [S2]. The experimental apparent contact angle for the injected droplet placed on the rough surface well matched with the theoretical apparent contact angle derived from Equation (6).

$$\cos \theta_{0P/0S} = \frac{\gamma_{PV/SV} - \gamma_{PL/SL}}{\gamma_{IV}} \tag{4}$$

$$\cos \theta_1 = -\frac{\gamma_{PL}}{\gamma_{LV}} \tag{5}$$

$$(\pi r + b)\gamma_{LV}\cos\theta' + (\pi r\gamma_{PL} + b\gamma_{SL}) + \pi r\gamma_{PL} + 2(h - \Delta h)\gamma_{PL} - (\pi r\gamma_{PV} + b\gamma_{SV}) = 0$$

$$= \cos\theta' = \frac{(\pi r\gamma_{PV} + b\gamma_{SV}) - 2(\pi r + h)\gamma_{PL} - b\gamma_{SL}}{(\pi r + b)\gamma_{LV}}$$
(6)

The surface tension of water (γ_{LV}) is ~72.8 mN/m, silicon (γ_{SV}) is ~61.22 mN/m, and silica (γ_{PV}) is ~57.71 mN/m [47]. Contact angles are extremely sensitive to contamination. It can be increased by the presence of an oxide layer or contaminants on the solid surface. The good approximation of the Young angle of silica (θ_{0P}) and silicon (θ_{0S}) is found to be 60 ± 20° and 38±4°, respectively, from the literature [48, S3]. Substituting these values into Equation (4), the interfacial tension force for the pillar (γ_{PL}) and substrate (γ_{SL}) has been calculated. The pinning angle (θ_{1}) has also been found from Equation (5) by putting the required values. Later, Equation (6) has been introduced to evaluate the theoretical apparent contact angle considering the penetration of water droplets into the grooves between the pillars, which is Wenzel wetting state. For the fabricated nanopillar geometry, the

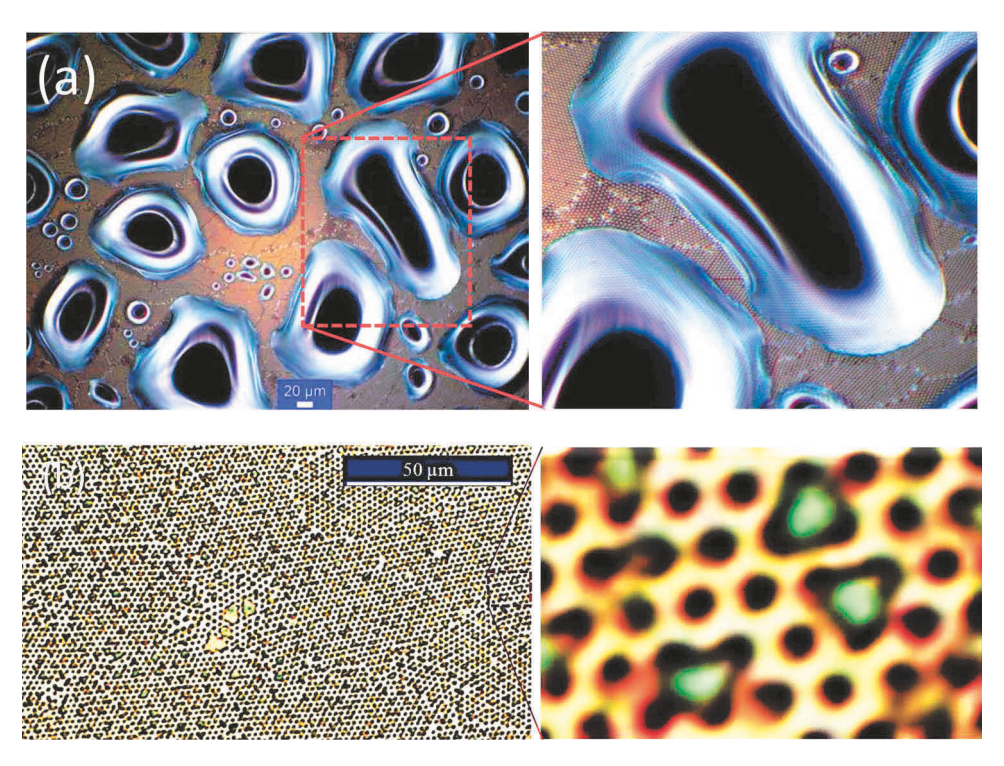


Figure 3. Wenzel wetting state was observed with irregular and pinned droplets [21]. Contact line pinning of the droplets is observed in (a). The condensed state of the droplets was zoomed to the unit cell.

designed parameters were—pillar radius, $r = 0.35 \, \mu m$, spacing, $b = 0.3 \, \mu m$, and height, $h = 0.3 \, \mu m$. The apparent contact angle was measured by placing a single droplet on the pillared surface as shown in Figure 4. The measured values of the apparent contact angle of water droplet on pillared surfaces (83 \pm 1.99°) showed good agreement with the derived values (~77°) from Equation (6) and the maximum deviation was observed to be ~7–8%. Although the wetting state of the injected droplet on the pillared surface was observed to be Wenzel state, it could not be described easily by the classical Wenzel equation [49], but showing excellent agreement with the approach [45] based on the balance of horizontal equilibrium interfacial tension forces of a droplet positioned on rough pillared surface [S2].

However, condensation test was conducted under different environmental conditions because humidity changes the supersaturation and the energetics of the nucleation [50, 51]. To elucidate the wetting state of the condensed droplets, microscopic image of condensation test was zoomed to a unit cell as shown in Figure 3b. The pinned and irregular droplets were observed. Directional anisotropy was also observed. It ensures that the condensed droplets found in the present study were in Wenzel state, which is well consistent to the literature [21, 32]. The bottom of the water droplet was not circular, and a three-phase contact line ended along the edge of the pillar as shown in Figure 3a.

Later, theoretical model of apparent contact angle has been formulated for condensed droplet based on the energetic state. To prevent coalescence, the energy required to overcome the capillary pressure ($E_{capillary}$) must be higher than the surface energy reduction (E_s) by coalescing of droplets [S4] mentioned in Equation (7) -

$$E_{capillary} \ge E_{S}$$
 (7)

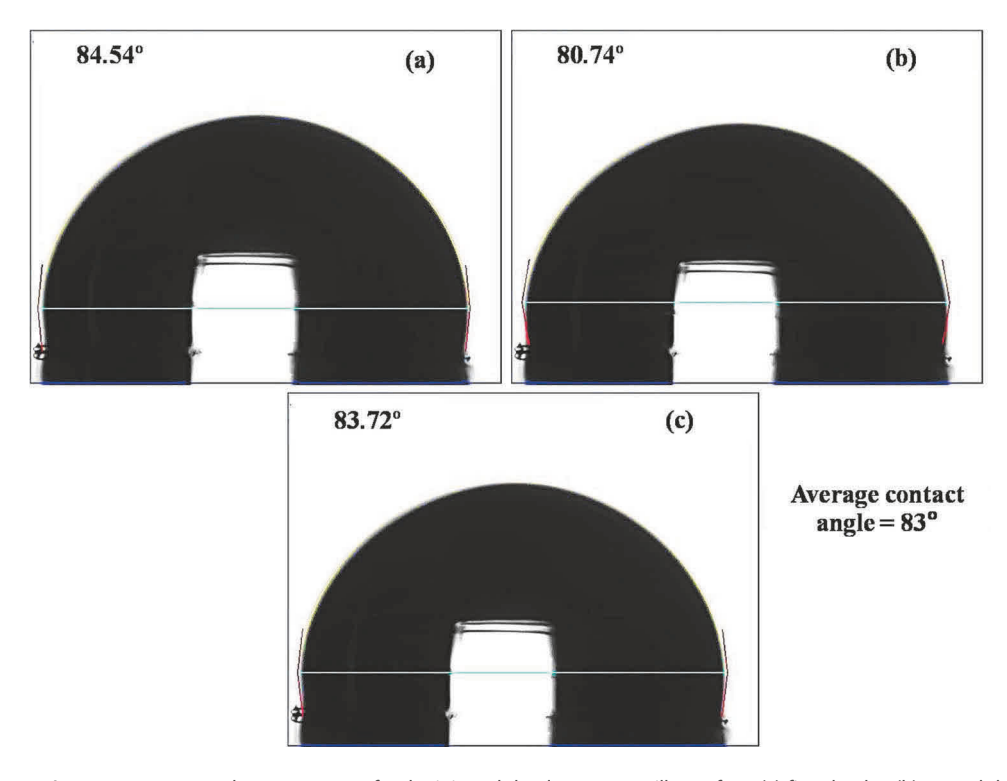


Figure 4. Apparent contact angle measurement for the injected droplet on nanopillar surface: (a) first droplet, (b) second droplet, and (c) third droplet. The average apparent contact angle was considered with 1.99° standard deviation.

The capillary energy was calculated from the work done by the volume of the water at the liquid-solid interface. It depends on capillary pressure $(P_{capillary} \approx 2\gamma_{LV}\cos\theta'/r)$ working at the interface multiplied by the volume of water (V), base area contact of a droplet (A), and the pillar density (α) . The pillar density (α) was assumed to be a function of pillar radius with a pitch of approximate 3r as shown in Figure 5. So, capillary energy equation can be written as follows:

$$E_{capillary} = P_{capillary} \times V \times \alpha \times A \tag{8}$$

In the present study, the pinned droplets were observed to be irregular shaped. For simplicity, the droplets were assumed to be the spherical cap. By definition, r_b is the base radius of the spherical cap, S is the height of the cap, and V_s is the volume of the cap, which all are related to the apparent contact angle mentioned in Equation (9) [52]. The surface area reduction from two coalescing droplets (R_1 and R_2) has been calculated based on the above assumption and the radius of the droplets are considered same ($R_1 = R_2 = R$). The reduction in surface energy (E_s) can be written as Equation (10). The minimum radius of the pillar required to pin the droplets as a function of pillar height (h) and apparent contact angle (θ') has been found from Equation (11)

$$S = R \times (1 - \cos \theta')$$

$$r_h = R \times \sin \theta'$$
(9)

$$V_s = \frac{\pi R^3}{3} (2 + \cos \theta') (1 - \cos \theta')^2$$

$$E_{\mathcal{S}} = \frac{2\pi R^2 \times \gamma_{LV} \times \sin^2 \theta' \times (2 - 2^{2/3})}{1 + \cos \theta'} \tag{10}$$

$$2\gamma_{LV}\cos\theta'\times\pi\times r\times h\times\alpha\times A\geq \frac{2\pi R^2\times\gamma_{LV}\times\sin^2\theta'\times(2-2^{2/3})}{1+\cos\theta'}$$

$$r \le 1.55 \times h \times \cos \theta' \times (1 + \cos \theta') \tag{11}$$

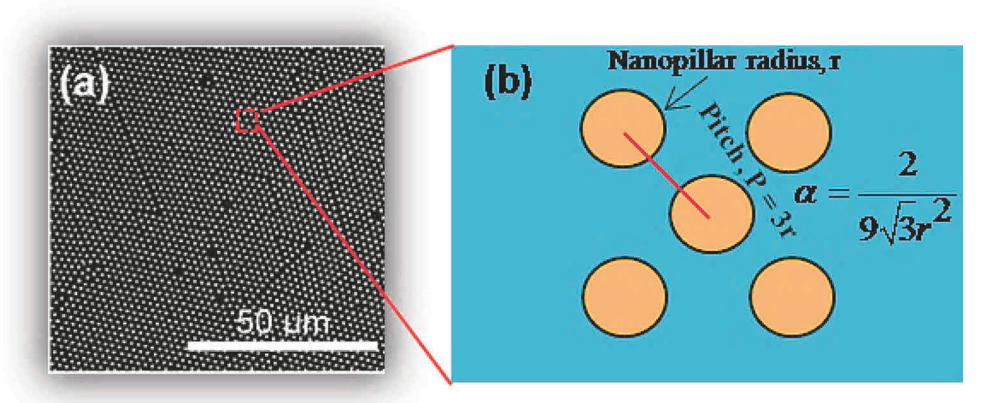


Figure 5. (a) Microscopic image of the nanopillar surface (top view). (b) Schematic of a portion of the nanopillar surface where five pillars have been arranged in a regular way. The center to center distance of the pillar (pitch) was approximated as P = 3r. The pillar density (α) was calculated based on the equation depicted in the figure.

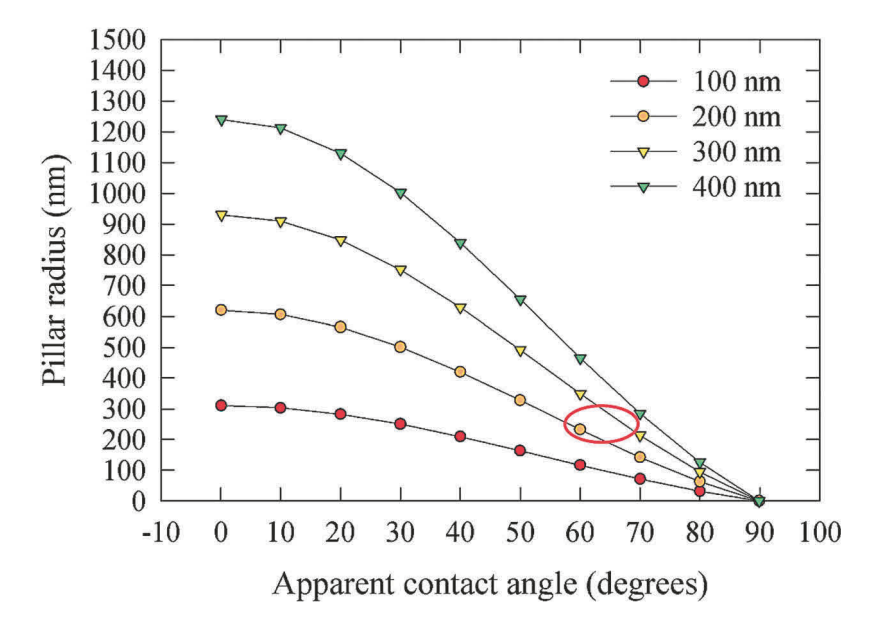


Figure 6. The pillar radius required for the energy to overcome the capillary pressure to equal the energy reduction from coalescence at varying apparent contact angles and pillar heights. The region of contact angle and pillar radius studied is shown with a solid circle.

In the present study, the fabricated pillar radius ($r = 0.35\mu m$) was within the limit depicted by Equation (11). As a result, the nanopillars exhibit droplet pinning behavior for a certain range of apparent contact angle based on the pillar height and spacing. For the present model, the apparent contact angle for the condensed droplet was observed to be $\sim 60-70^{\circ}$ for 0.30 μm pillar height as shown in Figure 6. The calculated apparent contact angle and images (Figure 3a and b) have elucidated the wetting state of the condensed droplet as "Wenzel state."

Droplet growth mechanism

The time-lapsed growth of droplets for both silicon and nanopillar surfaces at 40% RH and 60% RH has been reported in Figures 7-9, respectively (Video S5, S6). Within the first 15 s, spherical droplets were seen for all surfaces. Regular spherical-shaped droplets were observed for the bare silicon surfaces at both humidities. The droplet dynamics changed significantly for the nanopillar surfaces. At t = 15 s, on nanopillar surfaces, droplets nucleated slowly and was observed to span along the pillars as shown in Figures 3b and 8a. Once droplets span multiple pillars they continue to grow by stretching. This is due to the extensive pinning caused by the pillars. This pinning effect alters the condensation dynamics (Video S7). Hence, non-spherical and asymmetrical droplets were observed on the nanopillar surface. This pinning effect of the droplets made it difficult for them to coalescence until they touched each other. Some of the droplets that developed without coalescing retain their spherical shape and grew through the direct condensation. During the 90 min recording, most droplets that contribute to coalescence events eventually lost their spherical shape and accelerate their growth. The droplet pinning on the surface did not prevent droplet growth or merging since droplets continue to grow due to direct condensation at the vapor-liquid interface. At 60% RH, the diameter of the condensed droplets was found larger than 40% RH as shown in Figure 9. The probable cause might be the increased mass of water vapor accumulation from the humid air into the vapor-liquid interface of the droplets. Condensed droplet's direct growth rate appeared to be

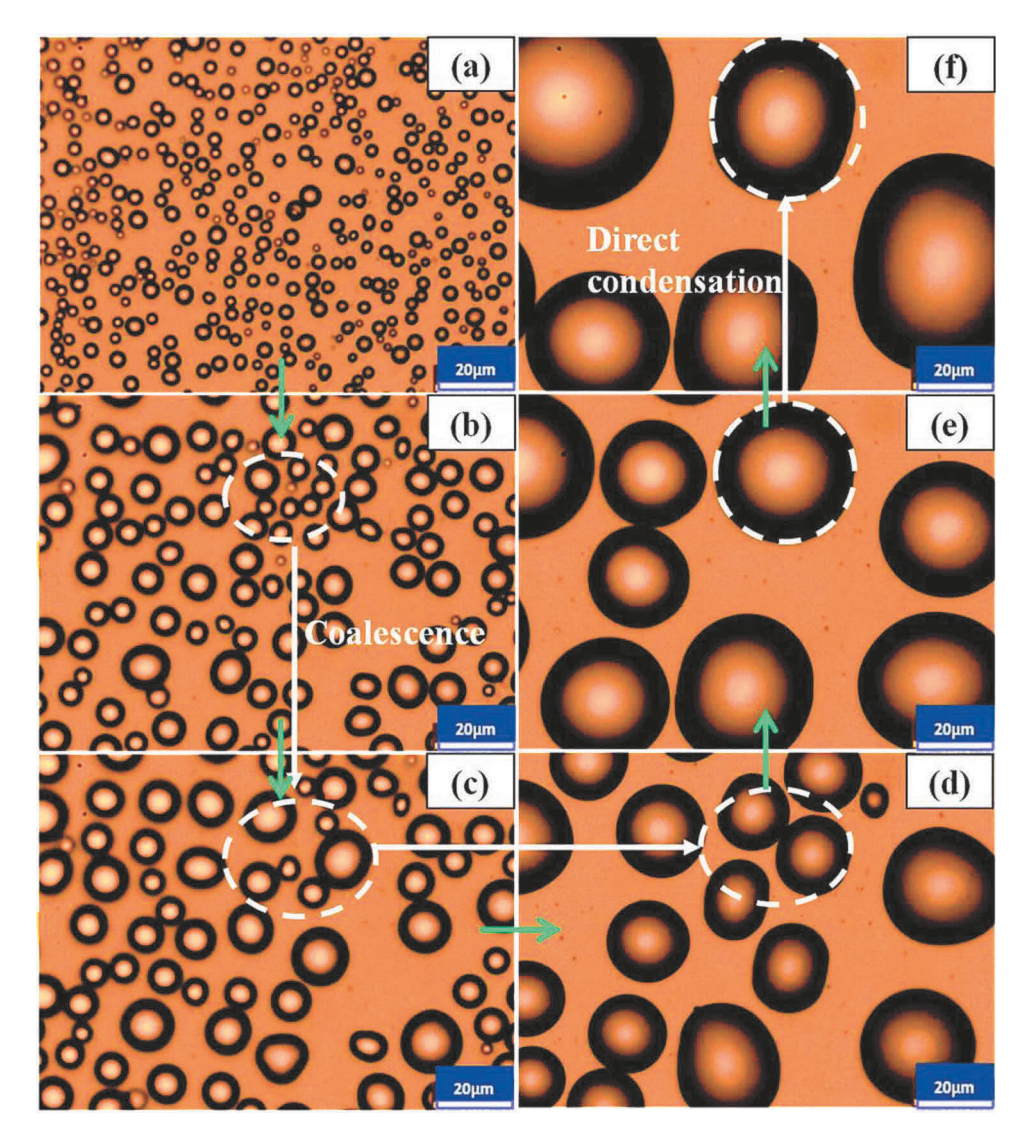


Figure 7. Early stage of condensation for silicon surface: (a) 15 s, (b) 45 s, (c) 1 min, (d) 2 min, (e) 3 min, and (f) 4 min at 40% RH. Images are $122.43 \times 91.83 \mu m$.

higher for silicon surface compared to nanopillar surface for all the considered time-lapse. The reason might be the absence of the components of the substrate thermal resistance to heat transfer offered by the nanopillars. As a result, it accelerates the direct growth of droplet and the higher coalescence rate was found for silicon surface evident from the supporting video S5. For both surfaces, at t = 120 s, lower droplet density and higher surface coverage were observed for 60% RH compared to 40% RH as shown in Figure 9. Although the lower direct growth rate was found for the droplets condensed on the nanopillar surface for a particular humidity, the pinning effect enhances the number of stable droplets on this surface compared to plain silicon surface over a time span. This higher density of the droplet over a specific time period signifies the importance of this fabricated nanopillar surface in long-term condensate harvesting [43, 44].

Figure 8. Early stage of condensation for nanopillar surface: (a) 15 s, (b) 45 s, (c) 1 min, (d) 2 min, (e) 3 min, and (f) 4 min at 40% RH. Images are $122.43 \times 91.83 \ \mu m$.

Mechanism of droplet regeneration

For silicon surface, droplet regeneration images have been recorded for different time-lapsed that were approximately 40 min apart as shown in Figures 10 and 11. Repeated coalescence and regeneration phenomenon have been observed on the surfaces. The regeneration of droplet was likely to be occurred at pre-coalesced space (void space) rather than bare spaces with no previous nucleation at 40% RH. This nature of droplet dynamics was also found to be similar for 60% RH. From Figure 12c and Figure 12e, the nucleated droplets approach nearly equal diameter within 1 min at two different time regions (~10 min lapse) elucidating nearly constant growth rate for the newly generated population at two different time zones. The same behavior of droplet growth rate was also observed in Figure 13b for the nanopillar surface where regeneration of droplet occurred in a void space created by pre-existing droplet that previously coalescence with neighboring droplets. The regeneration of droplets appeared as a cluster of tiny droplets and their center was located very close to each other. At the same time, they grew very quickly along multiple

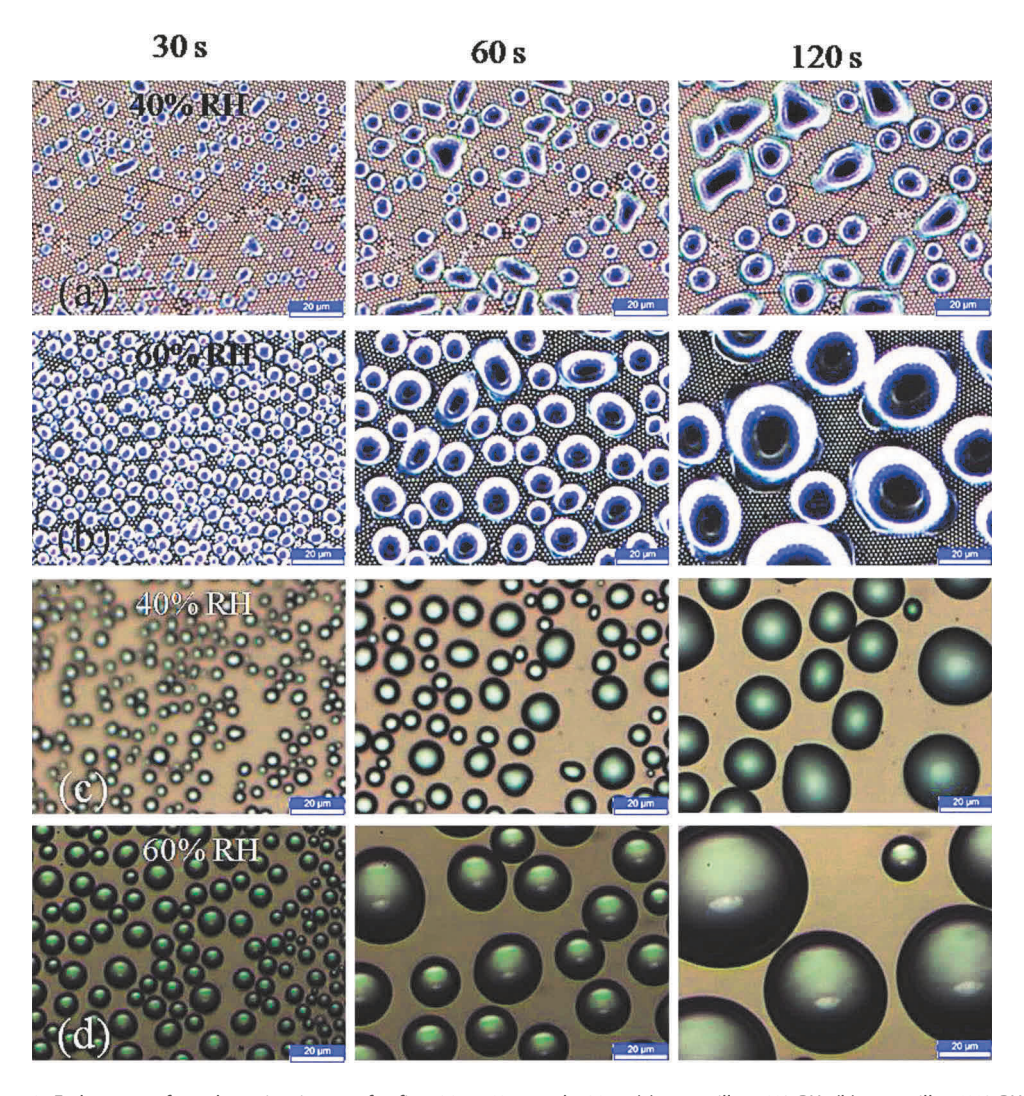


Figure 9. Early stage of condensation images for first 30 s, 60 s, and 120 s: (a) nanopillar-40% RH, (b) nanopillar-60% RH, (c) silicon-40% RH, and (d) silicon-60% RH. Images are 122.43 \times 91.83 μ m.

directions and turned into arbitrary shape within 60 s. Less time is required for the rebirth of the droplets from ambient environment on the silicon surface as shown in Figure 14. From the time-lapsed images, just before the first regeneration, the coalescence happens and triggers the rejuvenation of droplets to relieve high surface energy. The nanopillar surface impedes coalescence rate, delaying the regeneration (less void creation compared to silicon surface) of droplet for both humidities as depicted in Figure 14. This confirms the larger stability (duration of stay) of the condensed water droplet on the nanopillared surfaces compared to silicon surface and eventually facilitates time management in better condensate harvesting for larger scale.

Effect of relative humidity (RH)

The effect of the nanopillars on the droplet pinning has already been described, as compared to a silicon surface, indicating the influence of nanopillars on droplet growth rate and size distribution. Relative humidity (RH) has the tremendous potential to regulate the nucleation energy barrier for the heterogeneous nucleation mentioned in Equation (1). Hence, RH not only controls the initial

Figure 10. Regeneration of droplets for silicon surface at 40% RH: (a) 6 min 30 s, (b) 6 min 45 s, and (c) 7 min. Images are $122.43 \times 91.83 \ \mu m$.

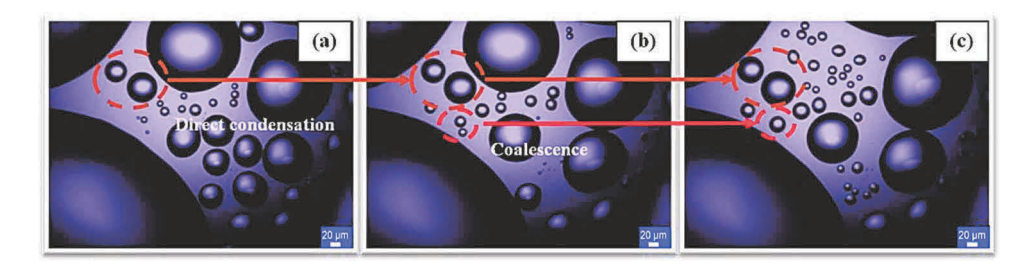


Figure 11. Droplet growth images for silicon surface at 40% RH: (a) 46 min, (b) 47 min, and (c) 48 min. The droplet growth at the middle stage of the test is also contributed by both coalescence (red dashed circle) and direct growth (brown dashed circle) phenomenon.

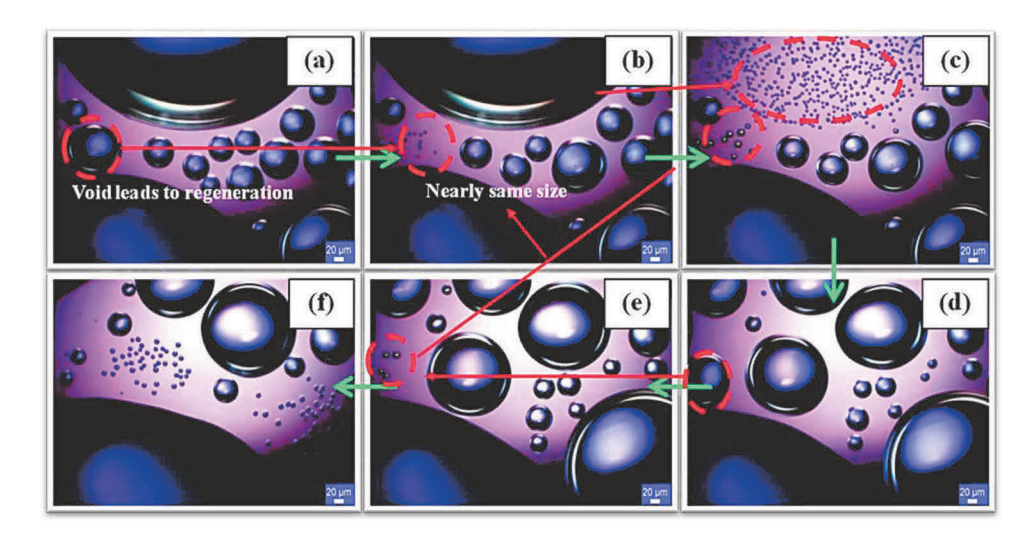


Figure 12. Droplet growth images for silicon surfaces at 60% RH: (a) 22 min 30 s, (b) 23 min, (c) 23 min 30 s, (d) 32 min, (e) 33 min, and (f) 34 min.

spatial and temporal distribution of the droplets on the condensing surface but also determine the subsequent growth rate of droplet for different applications. The influence of moisture content on the droplets dynamics is of relevance for several engineering applications such as larger water recovery system [43, 44]. Increasing the relative humidity during condensation test significantly influences the size distribution of the droplets on the nanopillar surface. Altering environmental conditions to 60% RH from 40% RH produces a noticeable increase in the droplet size within the

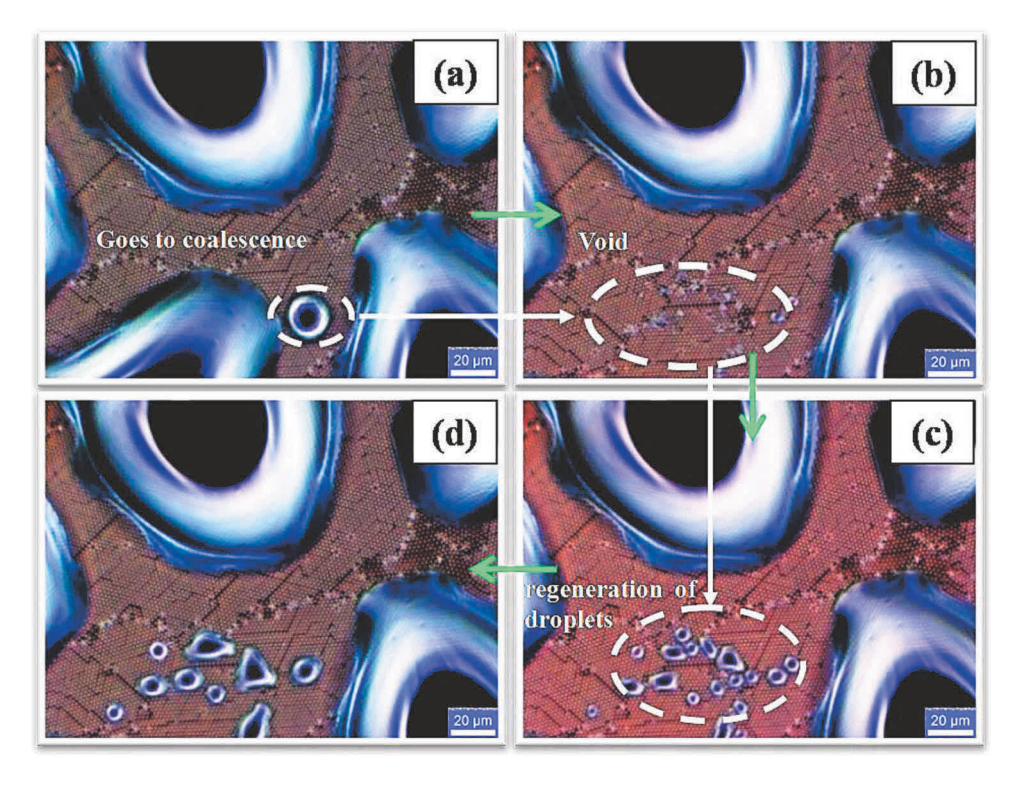


Figure 13. Regeneration of droplets for nanopillar surface at 40% RH: (a) 19 min 30 s, (b) 20 min, (c) 20 min 30 s, and (d) 21 min.

90 min video recording. During the early phase of condensation (first 10 min), the average diameter of the formed droplets can be modeled by power-law growth. The growth of droplets on nanopillar surfaces for first 10 min can be governed by $d \propto t^{0.56}$ and $d \propto t^{0.68}$ equations for 40% RH and 60% RH, respectively, as shown in Figure 15a and b. However, during the experiment, many droplets swept out of the frame. The maximum average diameter of the droplet was found ~150 μm for 60% RH. The probable cause for this larger growth might be the higher amount of water vapor accumulation from the high humid air at the growth interface of the droplet. The mass transfer across the vapor-liquid interface under certain relative humidity [13, 53] can be expressed as Equation (12)-

$$m'' = \phi(T_{sat} - T_s) \tag{12}$$

where Tsat is the saturation temperature of the system (varies with RH), m"is the mass transfer rate across the interface, ϕ represents the kinetic mobility, which can be found from Equation (13):

$$\phi = \frac{2\beta}{2 - \beta} \frac{h_{fg}}{\sqrt{2\pi R_m T_{sat}}} \frac{1}{(1/\rho_G - 1/\rho_D) T_{sat}}$$
(13)

 β is the constant that ranges from 0.04 to 1 depending on the fluid [13]. In the present experimental condition, β is assumed to be "1" similar to the literature [53]. Considering Equation (12), ~12.5× higher mass transfer through the vapor-liquid interface was found for 60% RH which significantly aids in condensate harvesting.

Additionally, to explore the effect of humidity, the growth of a single droplet on silicon surface at 40% RH and 60% RH has been recorded in Figure 16. A lot of coalescence events were seen.

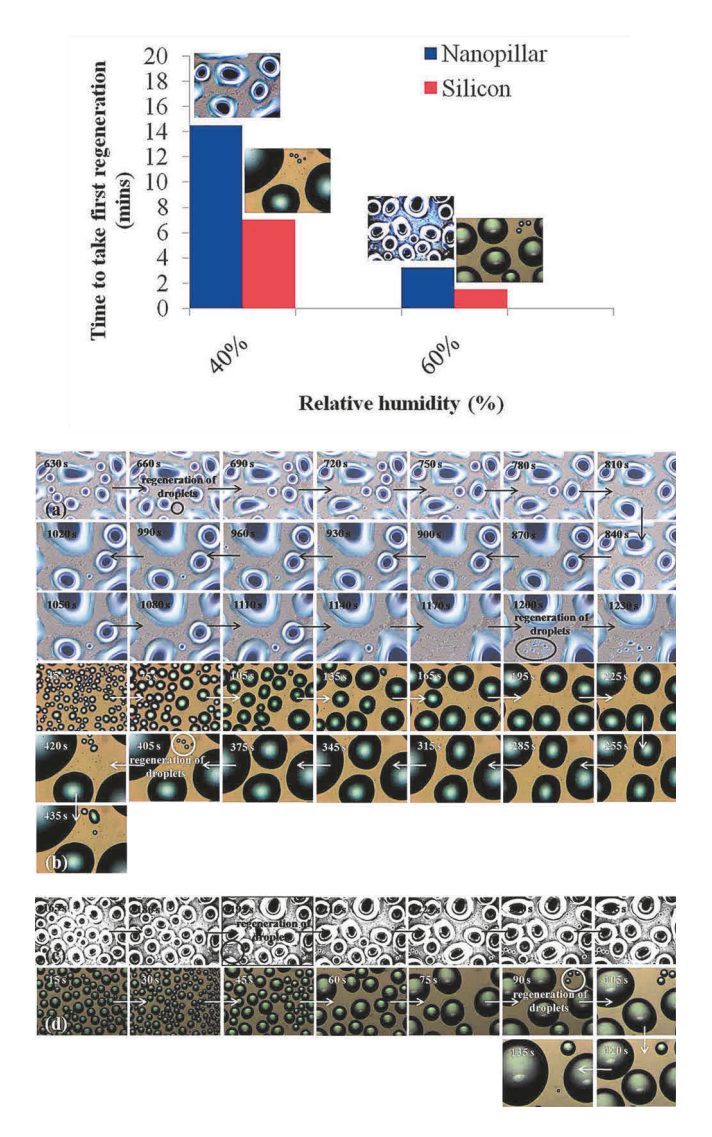


Figure 14. Time to reach first regeneration. Time-lapse images for different cases up to first regeneration. The regeneration of droplets was seen to be delayed by the patterned surface for both humidities. The pinning of droplets made the droplet less movable (water stability and more time for water collection): (a) nanopillar-40% RH, (b) nanopillar-60% RH, (c) silicon-40% RH, and (d) silicon-60% RH. Images are $122.43 \times 91.83 \mu m$.

However, 40% RH exhibits \sim 6× time delay to reach an equivalent diameter (\sim 70 µm) of a droplet compared to 60% RH keeping all other experimental variables constant.

Effect of different surfaces on droplet growth

To understand the relative significance of coalescence phenomenon over direct condensation, local growth dynamics of the individual droplet was carried out for both surfaces. The arbitrary droplets were tracked on silicon and nanopillar surface under the same condition over the first 600 s of the test as shown in Figure 16a and Figure 17a, respectively. In Figure 16, the dominance of small coalescence events on droplet's final diameter was observed for silicon surface. Interestingly, for nanopillar surface, both of the tracked droplets underwent three large coalescence events during

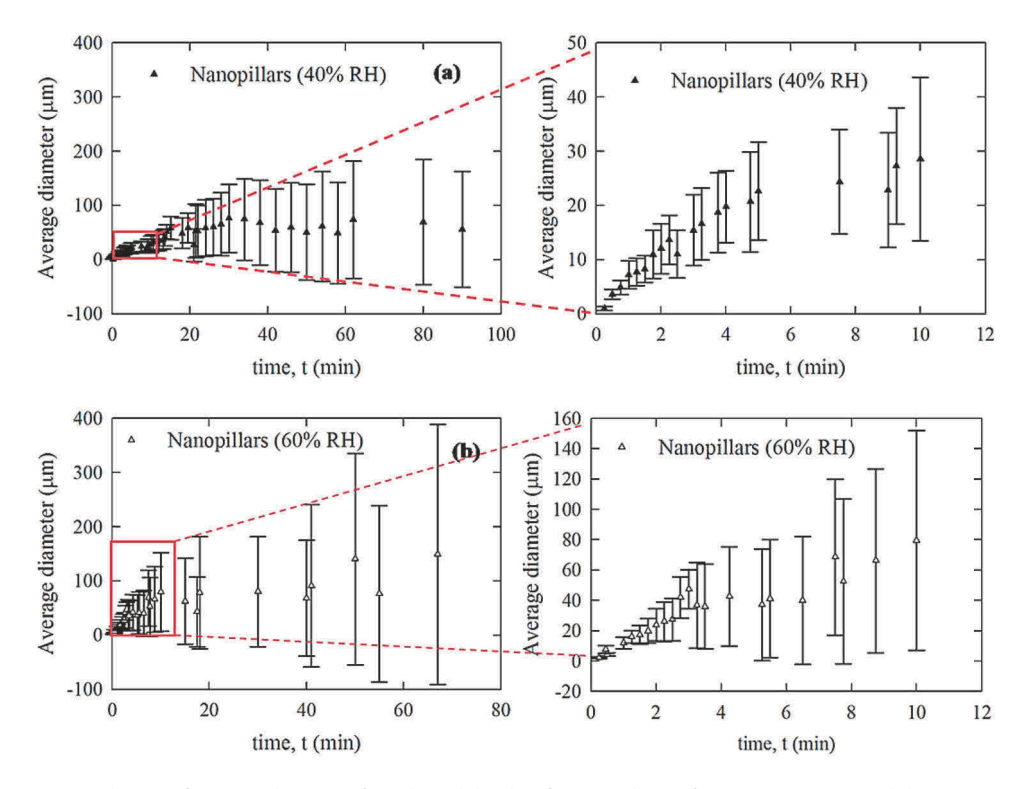


Figure 15. Distribution of average diameter of condensed droplets for nanopillar surfaces at (a) 40% RH and (b) 60% RH.

their growth within this time span to reach an equivalent diameter (\sim 65 µm). The rest of the period, direct condensation happened. However, the final diameter of the tracked droplet within first 600 s was dominated by large coalescence events. The direct growth was subdivided into three phases before facing each of the large coalescence events. During the first phase of direct condensation, the droplet diameter increased according to power law growth, $t^{\circ.80}$. At later stages, growth rate reduces to $t^{\circ.12}$, indicating lower direct condensation rate for the larger droplets. The reason might be the higher conduction resistance (R_d) offered by the unit area of the larger growing droplet [13, 54] as indicated by the Equation (14)-

$$R_d = \frac{R\theta'}{4K_w \sin \theta'} \tag{14}$$

The second droplet was tracked in Figure 17b. By investigating the local growth behavior of the two individual tracked droplets, the present study have found that individual droplet growth is not consistent with the progression of time as well as it significantly depends on the surrounding droplet's position and size (whether larger or smaller). Moreover, the nanopillar surface pins the droplets and prevents them from coalescing.

For global growth of the droplet, within the first 5 min of condensation, the number of droplets reduced according to power law decay as shown in Figure 18a. Decay equations $n \propto t^{-2.04}$ and $n \propto t^{-1.5}$ can be well fit for silicon and nanopillar surface, respectively, at 40% RH. This decrease in droplet density was found less significant for the nanopillar surface with the elapsed time compared to the silicon surfaces due to pinning effect. Pinning deters the rate of coalescence events. This leads to a relatively higher number of droplets on the nanopillars surfaces compared to silicon surface as coalescence event reduces the total number of droplet for a fixed frame. However, coalescence events were dominated for the silicon surface from the

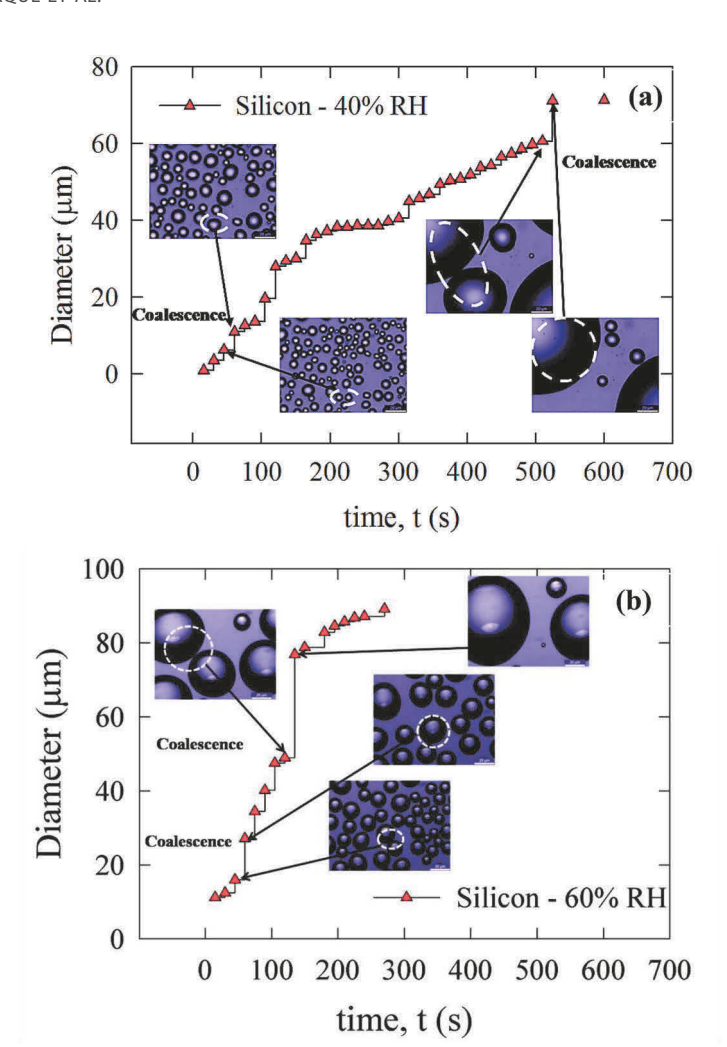


Figure 16. A droplet diameter growth with time for silicon surface at (a) 40% RH and (b) 60% RH.

beginning of the test, reducing the total number of droplets on the surface as large matured droplets covered most of the surfaces shown in Figure 18a. Due to coalescence events, the droplet diameter increased, enhancing dynamic interaction of the droplets at the liquid-solid surface. Frequent droplet sweeping was also observed for the silicon surfaces as visualized by the discontinuous shape of the Figure 18b compared to nanopillar surface. Within the first 10 min of condensation, the growth relationship can be modeled by $d \propto t^{0.91}$ for silicon and $d \propto t^{0.56}$ for nanopillar surfaces as shown in Figure 18b. For instance, the average diameter of the droplet was found ~52 µm for silicon surface at t = 5 min while ~10 min were required for the nanopillar surface to reach a diameter of ~30 µm as shown in Figure 18b.

The surface coverage is defined as the ratio of accumulated droplet's projected area to the substrate total area. As the total area of the droplets is largely dependent on the diameter and number of droplets, surface coverage was expected to be higher for nanopillar surface compared to silicon for the considered time-lapsed. For 50 min of condensation test, ~12.87% and ~24.13% increment of surface coverage was observed for nanopillar surface compared to silicon surface as shown in Figure 19a. At the same time, for both surfaces, it required ~3× higher time for 40% RH to

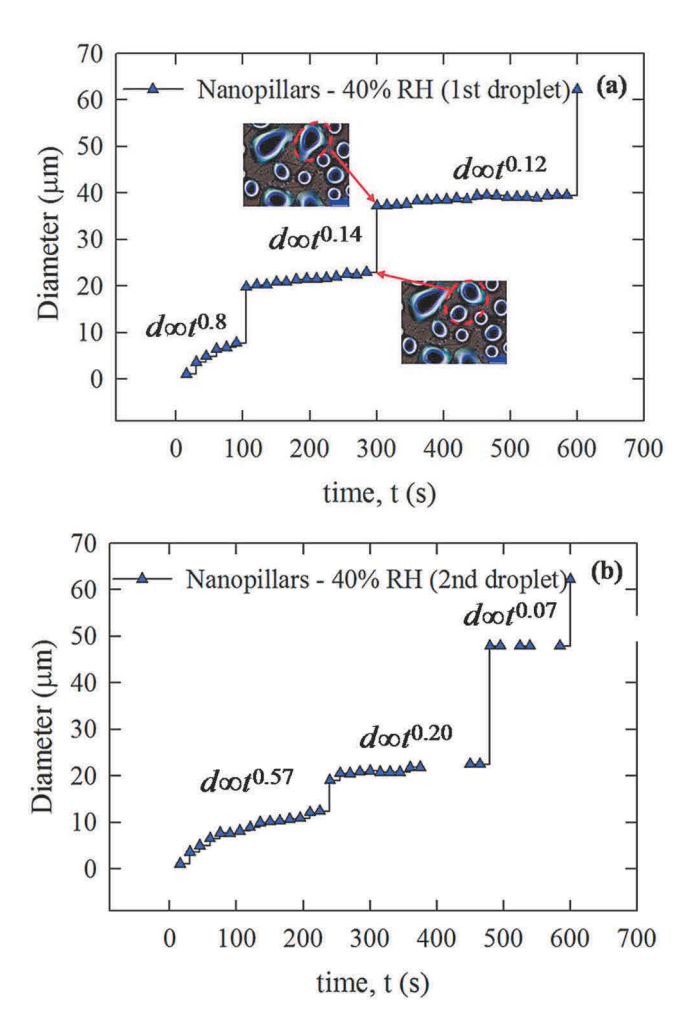


Figure 17. Individual droplet diameter growth with time: (a) first droplet and (b) second droplet for nanopillar surface at 40% RH.

reach a surface coverage equivalent to 60% RH. Hence, relative humidity accelerated the surface coverage that enhances the condensate harvesting significantly. The number of droplets per unit substrate area is defined as droplet density. Droplet density was found higher for nanopillar surfaces for a longer time period from the start of condensation test. Initial droplet density $10^8/\text{cm}^2$ found in this research is well consistent with the literature [17]. By pinning droplets, coalescence is suppressed for the nanopillar substrate and increases the droplet density significantly compared to silicon surface until the surface was almost found to be saturated (~80%) by the condensed droplets. For 40% RH, at later stages of condensation, the pinning effect of nanopillar made the droplets longer stable and less dynamic resulting in less bare space available for further renucleation. Again, sweep off of droplets occurred more spontaneously on the silicon surfaces creating more void spaces for the further renucleation of new droplets compared to nanopillar surface. Hence, at the later stage of the condensation test, higher droplet density was observed for silicon substrate as shown in Figure 19b. However, at this stage, the average diameter of droplets seems very comparable for both of the surfaces observed from Figure 18b.

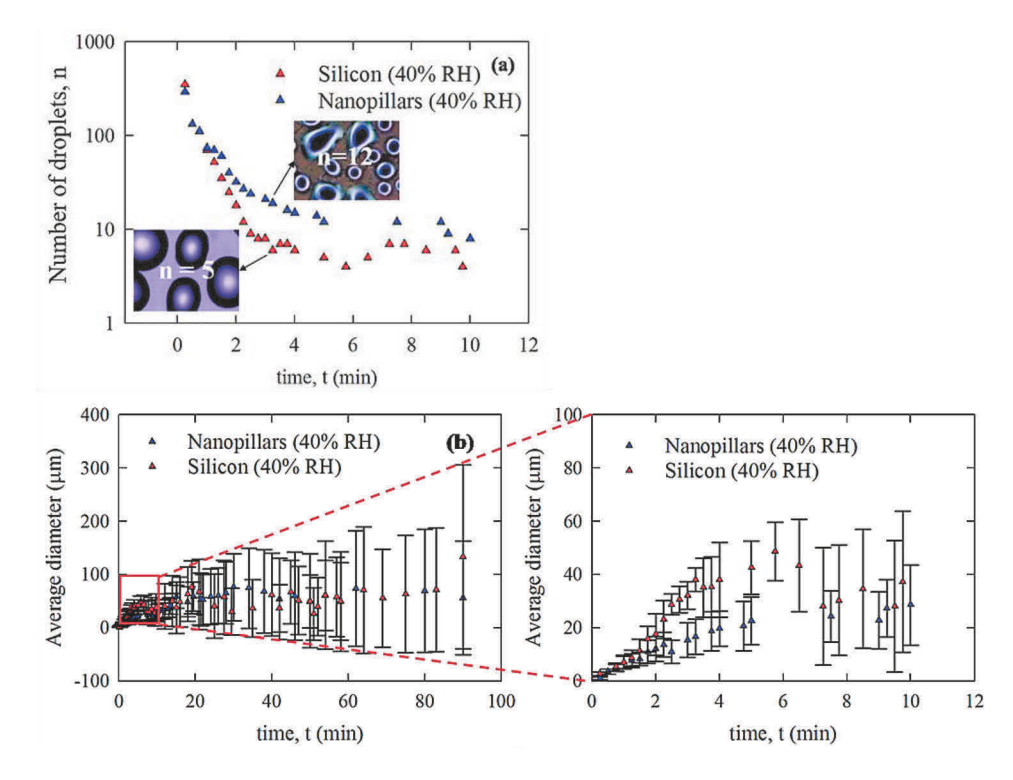


Figure 18. Distribution of (a) number of droplets at t = 10 min and (b) average diameter at 40% RH for the different surface.

Transient characteristics of droplet size distribution

The condensation dynamics were quantified based on the statistics of droplet distribution. Droplet size distributions for the initial nucleation period at 15 s have been reported in Figure 20. A wide range of droplet sizes was observed on the condensing surface, and this distribution reflects the instantaneity in the process of droplet growth. Figure 20 demonstrated the initial stage of droplet number and size that could be correlated with a lognormal distribution, well consistent with the literature [8]. At first, the droplets were uniform for nanopillar substrate. The dominant size of the droplet ranges 1-1.5 μm (40% RH) and 2-2.5 μm (60% RH). A larger number of smaller droplets appeared for the nanopillars and 60% RH recorded relatively larger sized droplets due to the higher volume of water vapor condensation from the humid air. Due to the strong pinning effect of the nanopillar, smaller droplets nucleated and became stable. Less number of larger sized droplets was observed for silicon surface compared to nanopillar surface. The dominant size ranges were found to be 2.5-3 µm (40% RH) and 12.5-15 µm (60% RH) for the silicon surface. The spatial distributions of droplet underneath the horizontal surface at time, t = 30, 58 min have also been reported in Figure 21. The maximum count of droplets was found within 0-25 μm diameter range for all the cases within 90 min of video recording. The exposed nanopillar surface exhibited bimodal distribution at 40% RH as shown in Figure 21a. The parent droplets were still there due to the pinning effect where the baby droplets contributed to the highest peak in the total droplet count. For silicon surface, droplet size range became wider. However, from Figure 21b, the right peak was not seen for the silicon surface and the distribution became unimodal.

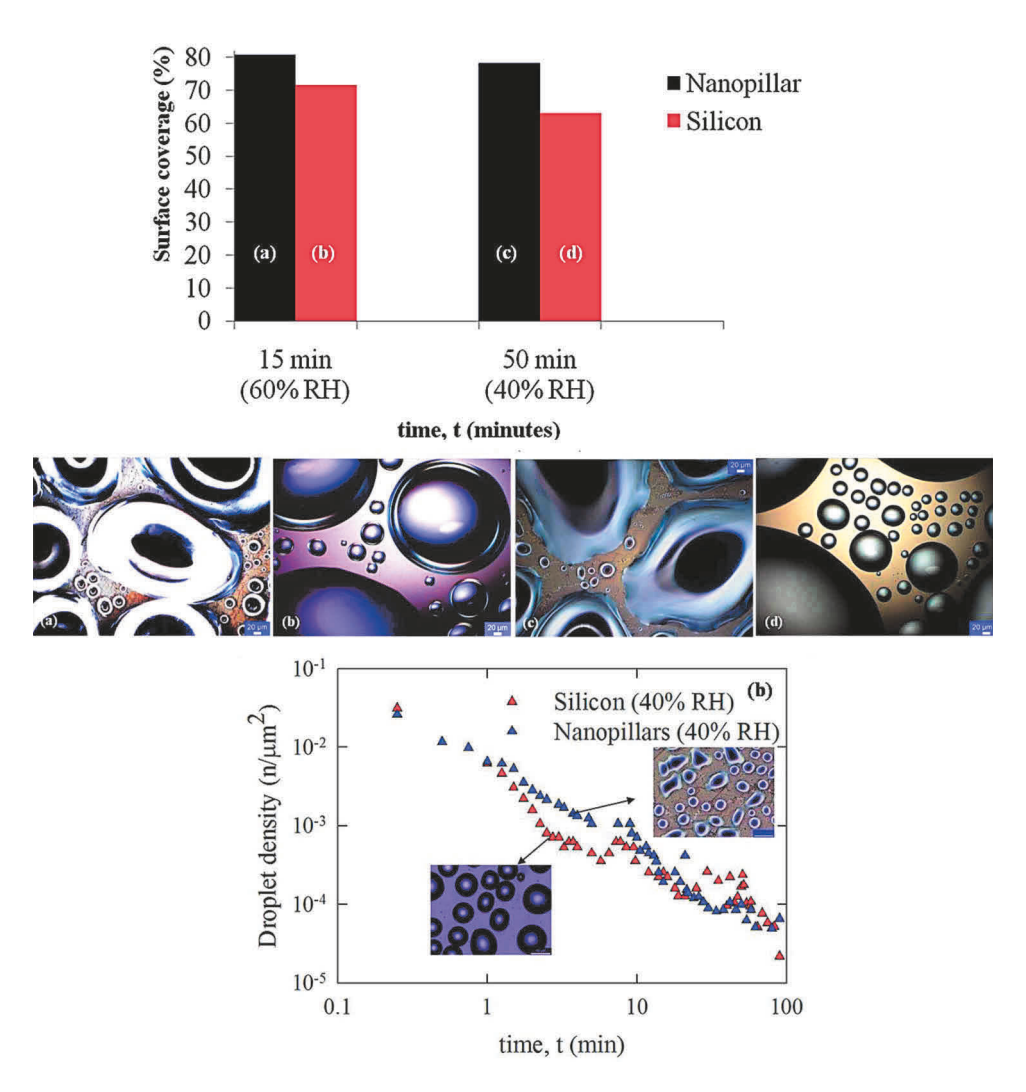


Figure 19. (a) Surface coverage for both of the surfaces at 60% RH and 40% RH, respectively. Nanopillar surface exhibits higher surface coverage compared to silicon surface for the considered frame area and time. This would aid significantly in doing the condensate droplet harvesting [43, 44], and (b) droplet density for different surfaces.

Conclusions

The manipulation of nucleation energy barrier for a droplet formation can be done either by altering the contact angle of water droplet on the surface or changing the relative humidity of the operating system. To resolve the effect of both contact angle and humidity, the imaging measurements in an environmental chamber have been conducted to understand the atmospheric condensation dynamics for silicon and nanopillar surfaces at different air-vapor mixture conditions. To explore the condensate harvesting, the video and image analysis has been implemented for detailed quantification. The droplet growth follows nucleation, direct growth, and coalescence events. The nanopillar surfaces have a significant impact on condensation behavior. By pinning droplets, coalescence is suppressed for the nanopillar surface and increases the droplet density significantly over a larger area that might yield higher surface coverage. The pinning state of the condensed droplets enhances the stability of the droplets on the nanopillar surfaces compared to the plain silicon surfaces. It

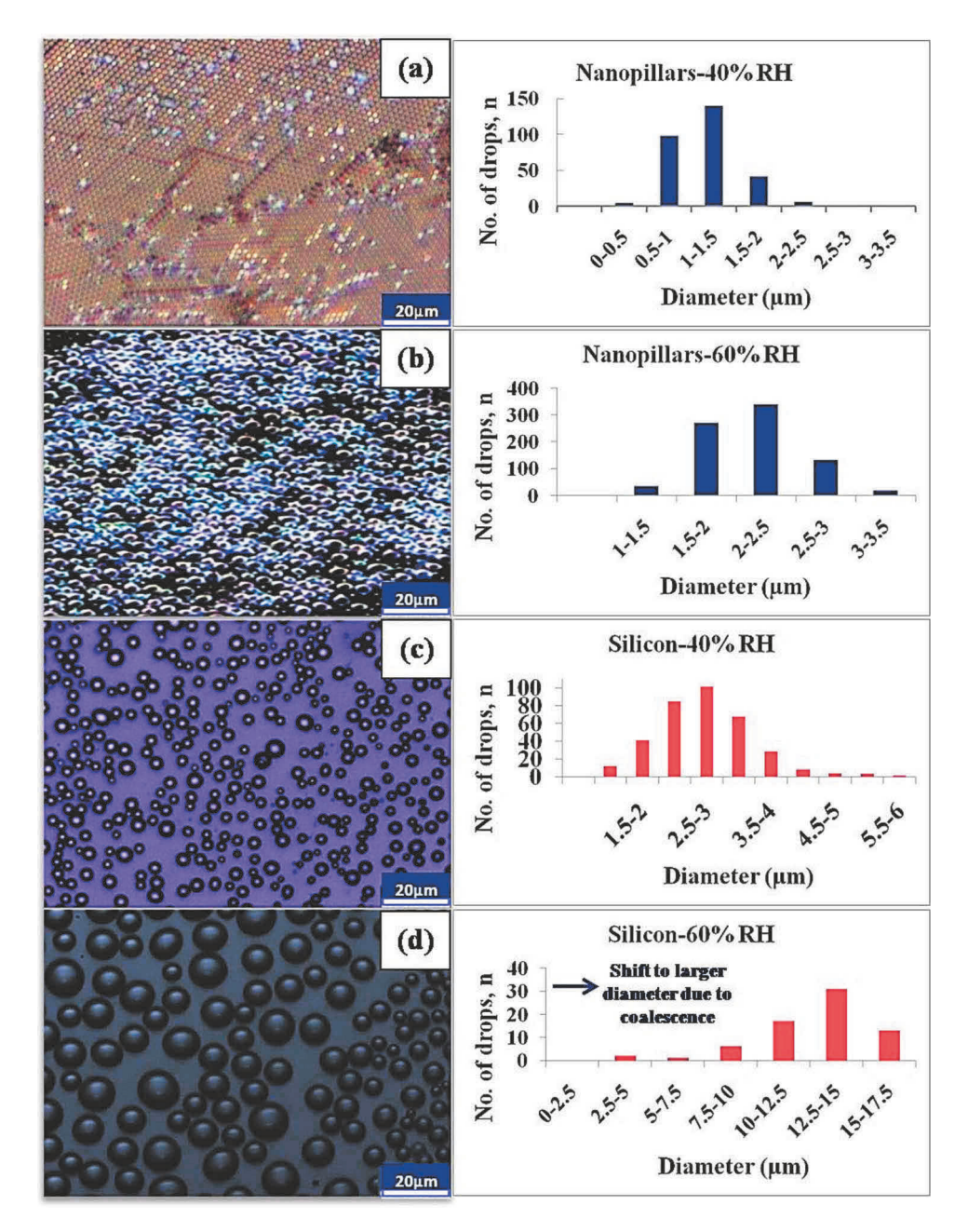


Figure 20. Distribution of droplet diameter at t = 15 s. Images are 122.43 \times 91.83 μ m.

significantly aids in time management for a large area condensate harvesting. However, droplets penetrate through the grooves in between the nanopillars and Wenzel state of the condensed droplet was observed. Additionally, increasing the humidity content in the atmosphere reduces the nucleation energy barrier, which is also favorable for larger condensate recovery. Maximum ~24.13% increment in condensate harvesting has been reported for the considered time span. During the early stage of condensation, the average diameter of droplet followed the power law growth and lognormal size distribution. At later stages, the distribution shifts to bimodal and unimodal. Coalescence events significantly contribute to the final diameter of the droplets that emerged on the nanopillar surface

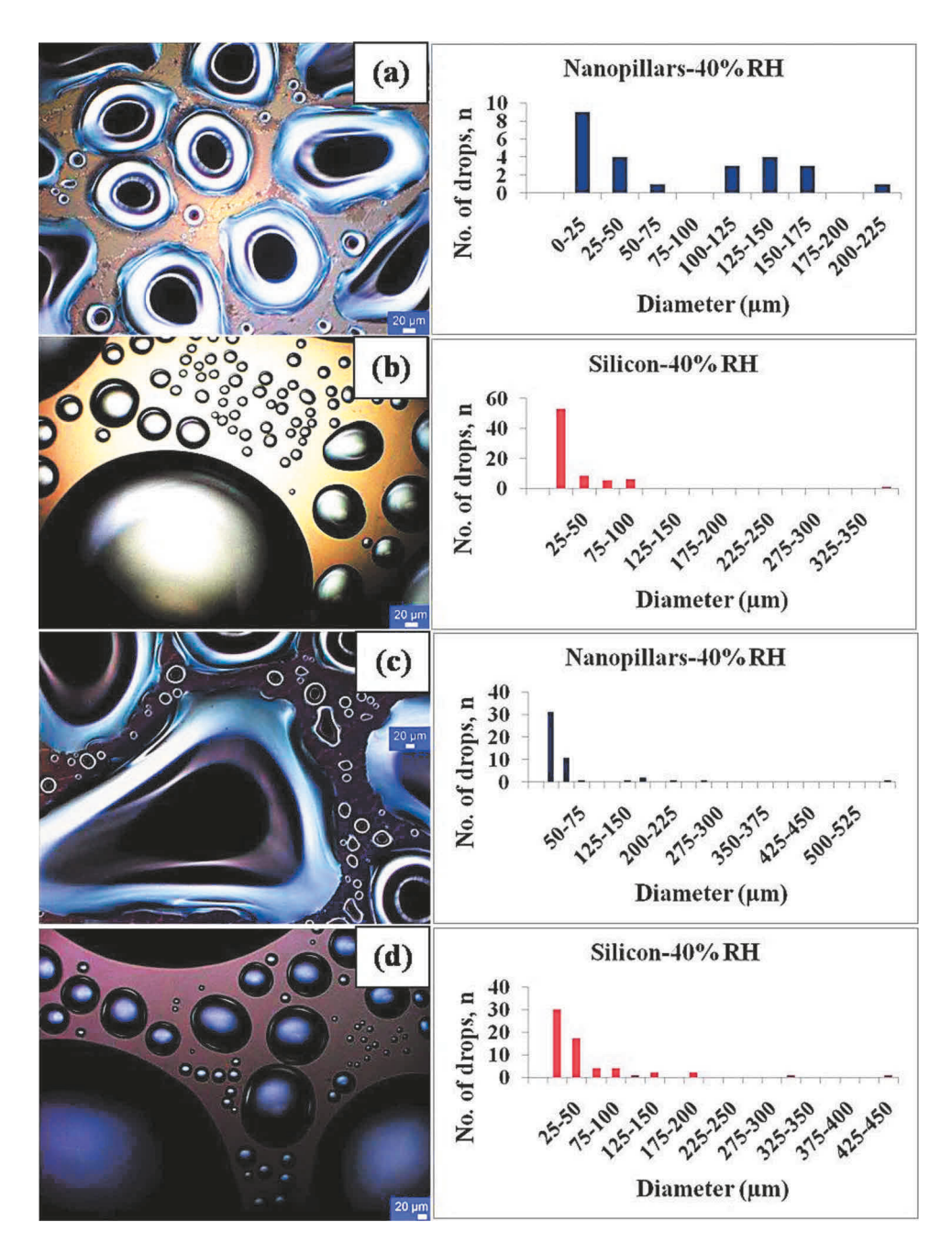


Figure 21. Distribution of droplet diameter at (a), (b) t = 30 min, and (c), (d) t = 58 min for different substrates at 40% RH.

within first 10 min. This provides insight for the role of coalescence events compared to the direct growth of condensed droplets for different surfaces. Moreover, from the initial period of the experiment, coalescence events are observed to be more frequent and spontaneous on the silicon surface and eventually reduce droplet density compared to a nanopillar surface. To summarize, this work shows how the nanopillar surface can effectively affect the nucleation energy, nucleation site density, droplet size distribution, and percentage of surface coverage under different ambient conditions.



Nomenclature

- contact area of a droplet, µm2 Α
- d diameter of droplet, um
- partial pressure of water vapor, Pa
- pressure of water vapor at saturation, Pa
- ΔG Gibbs free energy, J
- pillar height, µm or nm h
- latent heat of vaporization, J/Kg
- thermal conductivity of water, W/m.K
- pillar radius, µm
- droplet cap base radius, µm
- R droplet radius, µm
- the gas constant, J/kg K R_m
- droplet conduction resistance, m² K/W
- S droplet cap height, µm
- time, s or min
- temperature, K
- T_s surface temperature, K
- saturation temperature, K
- liquid droplet temperature, K
- volume of water in a gap, μm³
- spherical cap volume, μm³
- X, Y defined variable

Greek Symbols

- pillar density, number of pillars/μm²
- β constant
- γ_{LV} surface tension of water in air, mN/m
- γ_{PL} surface tension of water with pillar, mN/m
- surface tension of water with substrate, mN/m γ_{SL}
- surface tension of pillar, mN/m
- γ_{SV} surface tension of substrate, mN/m
- surface coverage %
- equilibrium contact angle, degree
- θ' apparent contact angle of droplet on pillar, degree
- θ_1 pinning angle of droplet by the pillar edge, degree
- droplet density, Kg/m³ ρ_d
- water vapor density, Kg/m³ ρ_G

Acknowledgments

The authors would like to thank Dr. Steve Eckels and the Institute for Environmental Research (IER) for the use of the environmental chambers. The authors also acknowledge their gratefulness to Rachel Bohm for her support in experimentation and both of the Universities for providing the required funding and facilities.

Funding

This material is based upon work supported by the US National Science Foundation under Grant Nos. 1509589, 1604183, and 1653792. Division of Chemical, Bioengineering, Environmental, and Transport Systems [1509589, 1604183, and 1653792].



Supporting Information

Additional information regarding the importance of relative humidity on heterogeneous nucleation energy barrier (S1), interfacial force balance (S2) to estimate the apparent contact angle (θ') considering the pinning from the pillar edge, contact angle on silicon surface (S3), unit calculation for energy equations (S4) as well as three videos showing the microscale droplet growth process (Video S5, S6), the pinning of droplets (Video S7) have been provided.

References

- [1] J. Rose, "Dropwise condensation theory and experiment: a review," Proceedings Institution Mechanical Engineers, Part. A: Journal Power Energy, vol. 216, pp. 115-128, 2002.
- [2] D. Beysens and C. Knobler, "Growth of breath figures," Phys. Rev. Lett., vol. 57, no. 12, pp.1433, 1986. DOI: 10.1103/PhysRevLett.57.1324.
- [3] A. Ashrafi and A. Moosavi, "Droplet condensation on chemically homogeneous and heterogeneous surfaces," J. Appl. Phys., vol. 120, no. 12, pp.124901, 2016. DOI: 10.1063/1.4962645.
- [4] M. Mei, F. Hu, C. Han, and Y. Cheng, "Time-averaged droplet size distribution in steady-state dropwise condensation," Int. J. Heat Mass Transf., vol. 88, pp. 338-345, 2015. DOI: 10.1016/j. ijheatmasstransfer.2015.04.087.
- [5] E. Le Fevre, "A theory of heat transfer by dropwise condensation," presented at the 3rd International Heat Transfer Conference, pp. 362-375, 1966.
- [6] M. Mei, B. Yu, M. Zou, and L. Luo, "A numerical study on growth mechanism of dropwise condensation," Int. J. Heat Mass Transf., vol. 54, no. 9, pp.2004–2013, 2011. DOI: 10.1016/j.ijheatmasstransfer.2011.01.002.
- [7] R. Narhe and D. Beysens, "Water condensation on a super-hydrophobic spike surface," EPL (Europhysics Letters), vol. 75, no. 1, pp.98, 2006. DOI: 10.1209/epl/i2006-10069-9.
- [8] B. S. Sikarwar, S. Khandekar, and K. Muralidhar, "Mathematical modelling of dropwise condensation on textured surfaces," Sadhana, vol. 38, no. 6, pp.1135-1171, 2013. DOI: 10.1007/s12046-013-0190-9.
- [9] J. E. Castillo, J. A. Weibel, and S. V. Garimella, "The effect of relative humidity on dropwise condensation dynamics," Int. J. Heat Mass Transf., vol. 80, pp. 759-766, 2015. DOI: ijheatmasstransfer.2014.09.080.
- [10] K. Yanagisawa, M. Sakai, T. Isobe, S. Matsushita, and A. Nakajima, "Investigation of droplet jumping on superhydrophobic coatings during dew condensation by the observation from two directions," Appl. Surf. Sci., vol. 315, pp. 212-221, 2014. DOI: 10.1016/j.apsusc.2014.07.120.
- [11] N. Miljkovic, R. Enright, and E. N. Wang, "Effect of droplet morphology on growth dynamics and heat transfer during condensation on superhydrophobic nanostructured surfaces," ACS Nano, vol. 6, no. 2, pp.1776-1785, 2012. DOI: 10.1021/nn205052a.
- [12] N. Miljkovic and E. N. Wang, "Condensation heat transfer on superhydrophobic surfaces," MRS Bulletin, vol. 38, no. 5, pp.397-406, 2013. DOI: 10.1557/mrs.2013.103.
- [13] R. Enright, N. Miljkovic, N. Dou, Y. Nam, and E. N. Wang, "Condensation on superhydrophobic copper oxide nanostructures," J. Heat Transfer, vol. 135, no. 9, pp.091304, 2013. DOI: 10.1115/1.4024424.
- [14] X. H. Ma, T. Y. Song, Z. Lan, and T. Bai., "Transient characteristics of initial droplet size distribution and effect of pressure on evolution of transient condensation on low thermal conductivity surface," Int. J. Thermal Sci., vol. 49, pp. 1517–1526, 2010. DOI: 10.1016/j.ijthermalsci.2010.05.011.
- [15] R. Wen, Z. Lan, B. Peng, W. Xu, and X. Ma, "Droplet dynamics and heat transfer for dropwise condensation at lower and ultra-lower pressure," Appl. Thermal Eng., vol. 88, pp. 265-273, 2015. DOI: 10.1016/j. applthermaleng.2014.09.069.
- [16] R. Narhe and D. Beysens, "Growth dynamics of water drops on a square-pattern rough hydrophobic surface," Langmuir, vol. 23, no. 12, pp.6486-6489, 2007. DOI: 10.1021/la062021y.
- [17] R. Leach, F. Stevens, S. Langford, and J. Dickinson, "Dropwise condensation: experiments and simulations of nucleation and growth of water drops in a cooling system," Langmuir, vol. 22, no. 21, pp.8864–8872, 2006. DOI: 10.1021/la061901+.
- [18] X. Qu, et al., "Self-propelled sweeping removal of dropwise condensate," Appl. Phys. Lett., vol. 106, no. 22, pp.221601, 2015. DOI: 10.1063/1.4921923.
- [19] S. Chavan, et al., "Heat transfer through a condensate droplet on hydrophobic and nanostructured superhydrophobic surfaces," Langmuir, vol. 32, no. 31, pp.7774-7787, 2016. DOI: 10.1021/acs.langmuir.6b01903.
- [20] M. M. Farhangi, P. J. Graham, N. R. Choudhury, and A. Dolatabadi, "Induced detachment of coalescing droplets on superhydrophobic surfaces," Langmuir, vol. 28, no. 2, pp.1290-1303, 2012. DOI: 10.1021/la203926q.
- [21] R. Enright, N. Miljkovic, A. A. Obeidi, C. V. Thompson, and E. N. Wang, "Condensation on superhydrophobic surfaces: the role of local energy barriers and structure length scale," Langmuir, vol. 28, pp. 14424-14432, 2012. DOI: 10.1021/la302599n.

- [22] N. Miljkovic, R. Enright, and E. N. Wang, "Modeling and optimization of superhydrophobic condensation," J. Heat Transfer, vol. 135, no. 11, pp.111004, 2013. DOI: 10.1115/1.4024597.
- [23] G. Li, et al., "Microscopic droplet formation and energy transport analysis of condensation on scalable superhydrophobic nanostructured copper oxide surfaces," Langmuir, vol. 30, no. 48, pp.14498-14511, 2014. DOI: 10.1021/la503003r.
- [24] D. Torresin, M. K. Tiwari, D. Del Col, and D. Poulikakos, "Flow condensation on copper-based nanotextured superhydrophobic surfaces," Langmuir, vol. 29, no. 2, pp.840-848, 2013. DOI: 10.1021/la304389s
- [25] K. O. Zamuruyev, et al., "Continuous droplet removal upon dropwise condensation of humid air on a hydrophobic micropatterned surface," Langmuir, vol. 30, no. 33, pp.10133-10142, 2014. DOI: 10.1021/
- [26] S. Anand, A. T. Paxson, R. Dhiman, J. D. Smith, and K. K. Varanasi, "Enhanced condensation on lubricantimpregnated nanotextured surfaces," ACS Nano, vol. 6, no. 11, pp.10122-10129, 2012. DOI: 10.1021/ nn303867v.
- K. Rykaczewski, et al., "Three dimensional aspects of droplet coalescence during dropwise condensation on superhydrophobic surfaces," Soft Matter, vol. 7, no. 19, pp.8749-8752, 2011. DOI: 10.1039/c1sm06219k.
- [28] J. Blaschke, T. Lapp, B. Hof, and J. Vollmer, "Breath figures: nucleation, growth, coalescence, and the size distribution of droplets," Phys. Rev. Lett., vol. 109, no. 6, pp.068701, 2012. DOI: 10.1103/ PhysRevLett.109.068701.
- [29] D. Attinger, et al., "Surface engineering for phase change heat transfer," A Review, MRS Energy & Sustainability-A Review Journal, vol. 1, E4, 2014 DOI:10.1557/mre.2014.9.
- [30] H. J. Cho, D. J. Preston, Y. Zhu, and E. N. Wang, "Nanoengineered materials for liquid-vapour phase-change heat transfer," Nat. Rev. Mater., vol. 2, pp. 16092, 2016. DOI: 10.1038/natrevmats.2016.92.
- [31] D. J. Preston, D. L. Mafra, N. Miljkovic, J. Kong, and E. N. Wang, "Scalable graphene coatings for enhanced condensation heat transfer," Nano Lett., vol. 15, no. 5, pp.2902-2909, 2015. DOI: 10.1021/nl504628s.
- [32] R. Wen, et al., "Wetting transition of condensed droplets on nanostructured superhydrophobic surfaces: coordination of surface properties and condensing conditions," ACS Appl. Mater Interfaces, vol. 9, no. 15, pp.13770-13777, 2017. DOI: 10.1021/acsami.7b01812.
- [33] R. Wen, et al., "Hydrophobic copper nanowires for enhancing condensation heat transfer," Nano Energy, vol. 33, pp. 177-183, 2017. DOI: 10.1016/j.nanoen.2017.01.018.
- [34] J. Huang, J. Zhang, and L. Wang, "Review of vapor condensation heat and mass transfer in the presence of noncondensable gas," Appl. Therm. Eng., vol. 89, pp. 469-484, 2015. DOI: 10.1016/j.applthermaleng.2015.06.040.
- [35] Y. Zhao, et al., "Effects of millimetric geometric features on dropwise condensation under different vapor conditions," Int. J. Heat Mass Transf., vol. 119, pp. 931-938, 2018. DOI: 10.1016/j. ijheatmasstransfer.2017.11.139.
- [36] H. Cha, et al., "Nanoscale-agglomerate-mediated heterogeneous nucleation," Nano Lett., vol. 17, no. 12, pp.7544-7551, 2017. DOI: 10.1021/acs.nanolett.7b03479.
- [37] J. B. Boreyko, et al., "Controlling condensation and frost growth with chemical micropatterns," Sci. Rep., vol. 6, 2016. DOI: 10.1038/srep19131.
- [38] J. C. Hulteen and R. P. Van Duyne, "Nanosphere lithography: a materials general fabrication process for periodic particle array surfaces," Journal Vacuum Science Technology A: Vacuum, Surfaces, Films, vol. 13, no. 3, pp.1553-1558, 1995. DOI: 10.1116/1.579726.
- W. Wu, A. Katsnelson, O. G. Memis, and H. Mohseni, "A deep sub-wavelength process for the formation of highly uniform arrays of nanoholes and nanopillars," Nanotechnology, vol. 18, no. 48, pp.485302, 2007. DOI: 10.1088/0957-4484/18/49/495102.
- [40] C. Qu and E. C. Kinzel, "Polycrystalline metasurface perfect absorbers fabricated using microsphere photolithography," Opt. Lett., vol. 41, pp. 3399-3402, 2016.
- [41] A. Bonakdar, et al., "Deep-UV microsphere projection lithography," Opt. Lett., vol. 40, pp. 2537–2540, 2015.
- [42] O. Shavdina, et al., "Large area fabrication of periodic TiO2 nanopillars using microsphere photolithography on a photopatternable Sol-gel film," Langmuir, vol. 31, no. 28, pp.7877-7884, 2015. DOI: 10.1021/acs. langmuir.5b01191.
- [43] H. Kim, et al., "Water harvesting from air with metal-organic frameworks powered by natural sunlight," Science, vol. 356, no. 6336, pp.430-434, 2017. DOI: 10.1126/science.aam8743.
- [44] A. Kajale, R. Peters, and M. Winslett, "Evaluation of effectiveness of condensate recovery and its reuse as a make-up water requirement in chilled water plants at the University of Alabama at Birmingham, ESTIMATION AND FORECASTING OF AIR HANDLING CONDENSATE RECOVERY USING MULTIPLE REGRESSION ANALYSIS AND TIME-SERIES AUTOREGRESSIVE MODELS," PhD thesis,1001, pp. 80, 2013.
- [45] S. Suzuki and K. Ueno, "Apparent contact angle calculated from a water repellent model with pinning effect," Langmuir, vol. 33, pp. 138-143, 2016. DOI: 10.1021/acs.langmuir.6b03832.
- [46] A. Ghosh, S. Beaini, B. J. Zhang, R. Ganguly, and C. M. Megaridis, "Enhancing dropwise condensation through bioinspired wettability patterning," Langmuir, vol. 30, no. 43, pp.13103-13115, 2014. DOI: 10.1021/la5028866.



- [47] A. Zdziennicka, K. Szymczyk, J. Krawczyk, and B. Jańczuk, "Some remarks on the solid surface tension determination from contact angle measurements," Appl. Surf. Sci., vol. 405, pp. 88-101, 2017. DOI: 10.1016/j. apsusc.2017.01.068.
- [48] I. T. Pai, C. Leu, and M. H. Hon, "A hierarchical structure through imprinting of a polyimide precursor without residual layers," J. Micromech. Microeng., vol. 18, no. 10, pp.105005, 2008. DOI: 10.1088/0960-1317/18/10/
- [49] R. N. Wenzel, "Resistance of solid surfaces to wetting by water," Ind. Eng. Chem., vol. 28, no. 8, pp.988-994, 1936. DOI: 10.1021/ie50320a024.
- [50] Q. Zeng and S. Xu, "Thermodynamics and characteristics of heterogeneous nucleation on fractal surfaces," J. Phys. Chem. C, vol. 119, pp. 27426-27433, 2015. DOI: 10.1021/acs.jpcc.5b07709.
- [51] A. Aili, Q. Ge, and T. Zhang, "How nanostructures affect water droplet nucleation on superhydrophobic surfaces," J. Heat Transfer, vol. 139, no. 11, pp.112401, 2017. DOI: 10.1115/1.4036763.
- [52] J. W. Harris and H. Stöcker, Handbook of Mathematics and Computational Science. New York, NY: Springerverlag New York, Inc., 1998.
- [53] D. Seo, S. Oh, S. Shin, and Y. Nam, "Dynamic heat transfer analysis of condensed droplets growing and coalescing on water repellent surfaces," Int. J. Heat Mass Transf., vol. 114, pp. 934-943, 2017. DOI: 10.1016/j. ijheatmasstransfer.2017.06.129.
- [54] H. Kim and Y. Nam, "Condensation behaviors and resulting heat transfer performance of nano-engineered copper surfaces," Int. J. Heat Mass Transf., vol. 93, pp. 286-292, 2016. DOI: 10.1016/j. ijheatmasstransfer.2015.09.079.